Simulation-Guided Design of Solar Steam Generator Arrays for Efficient All-Cold Evaporation under Natural Sunlight

Ke Shao [a], Jingjing Li [a], Jun Zhao [a], Suxu Wang [a], Yi Lu [b], Petri Murto [c,d], Zhihang Wang*[,e,f] and Xiaofeng Xu*[,a]

[a] College of Materials Science and Engineering, Ocean University of China, Qingdao 266100, China.

[b] Jiangsu Co-Innovation Center of Efficient Processing and Utilization of Forest Resources, International Innovation Center for Forest Chemicals and Materials, College of Science, Nanjing Forestry University, Nanjing 210037, China

[c] Department of Chemistry and Materials Science, Aalto University, Kemistintie 1, 02150 Espoo, Finland.

[d] Yusuf Hamied Department of Chemistry, University of Cambridge, Cambridge, CB2 1EW, United Kingdom.

[e] School of Engineering, College of Science and Engineering, University of Derby, Markeaton Street, Derby DE22 3AW, United Kingdom.

[f] Department of Materials Science and Metallurgy, University of Cambridge, Cambridge, CB3 0FS, United Kingdom.

* Corresponding authors: X. Xu, email: xuxiaofeng@ouc.edu.cn

Z. Wang, email: zw428@cam.ac.uk

ABSTRACT: Solar-powered interfacial evaporation has emerged as a promising, sustainable technology for clean water production with its minimal carbon footprint. Currently, extensive research efforts focus on enhancing solar evaporation rates and broadening the applicability of three-dimensional (3D) interfacial steam generators (SGs). For large-scale water production, individual 3D SGs must be integrated into system-level SG arrays for deployment in portable devices or solar distillation plants. Therefore, the SG array's configuration plays an even more critical role in boosting solar evaporation. From a methodological perspective, the development of numerical simulation and evaluation methods to predict the solar evaporation of SG arrays is an emerging research frontier. Nonetheless, the complex energy-water-solute interactions within SG arrays remain largely underexplored. Herein, 3D SGs and their integrated SG arrays are developed. The temperature, relative humidity, airflow and air particle distributions throughout individual SGs and SG arrays are simulated, guiding the optimization of SG structures and the arrangement of SG arrays. By promoting cold evaporation, 8-Fin SG achieves the highest water evaporation rate of over 2.3 kg m^{-2} h^{-1} under 1 sun, with a further increase to 4.8 kg m^{-2} h^{-1} under a moderate airflow, positioning it among the best-performing solar-powered SGs. The circular array configuration of nine 8-Fin SGs (12 cm spacing) enables sustained “all-cold evaporation” in each unit, where continuous energy harvesting from both ambient air and bulk water drives an exceptional evaporation rate of 5.9 kg m^{-2} h^{-1} of the SG array under natural sunlight. We present an integrated approach combining numerical simulation with experimental studies of SG and their arrays, inspiring a new paradigm for advancing SG arrays toward system-level applications.

KEYWORDS: *interfacial steam generation, photothermal materials, photothermal arrays, solar interfacial evaporation, solar distillation*

INTRODUCTION

Freshwater scarcity represents a critical and escalating challenge for human society, driven by multiple interrelated factors such as rapid population growth, urbanization, unsustainable water resource allocation, and intensifying climate change.[1] Currently, an estimated 1.8−2.9 billion people experience severe freshwater shortages for at least four months annually, with projections indicating a worsening crisis. By 2050, global freshwater demand is expected to increase by 19%, leaving 75% of the global population facing clean water scarcity.[2] Ensuring a consistent and reliable supply of clean water is thus an urgent global imperative. In response, advanced water purification technologies, including membrane filtration, thermal distillation, and reverse osmosis, have been developed over recent decades. While these innovations show promise, critical challenges persist, particularly concerning their energy consumption, operational costs, water treatment efficiencies and environmental impacts. Hence, addressing these gaps is essential to achieving sustainable solutions.[3, 4]

The sun serves as a primary source of renewable energy for our planet. Recent advancements in solar-powered interfacial evaporation have positioned this technology as a sustainable solution for water treatment.[5, 6] Its low-maintenance, grid-independent and user-friendly nature makes it particularly beneficial for producing portable clean water in remote, arid, and semi-arid regions.[7-9] Innovative strategies such as environmental energy harvesting, vaporization enthalpy recycling and salt-rejecting have enabled water evaporation rates to exceed the theoretical upper limit of brine.[7, 10, 11] The rational design and controlled fabrication of photothermal composites in three-dimensional (3D) monolithic forms (i.e., aerogels, hydrogels and sponges/foams) — featuring micro- and macro-scale attributes like structural elements, configuration, and porous architectures — has garnered significant research interest.[12-16] Particularly, 3D interfacial steam generators (SGs) are highly desired for their ability to synergistically enhance clean water production and support hybrid applications such as all-day

operations, zero liquid discharge, photosynthesis and environmental stimuli response.[15, 17-26]

The unique functionalities of 3D SGs arise from the intricate distributions of energy, water and salts within their structural components and device configurations.[27-30] Thermal energy distribution critically determines energy losses and gains on evaporation surfaces, while water supply and directional diffusion govern thermal management, salt rejection and evaporation rates.[8] Additionally, the porous structure and pore size distribution can be precisely modulated to enhance effective evaporation areas, steam release interfaces and cold evaporation zones. Rational fabrication of 3D SGs with multiscale hierarchical structures not only minimizes material consumption but also eliminates "dead evaporation zones".[31, 32] As a result, the operation of 3D SGs represents a complex, multi-physical-field coupled process. However, due to the structural diversity of 3D SGs across applications, the correlations between energy, water and salts remains highly dependent on specific structural designs and device configurations, rendering it challenging to generalize. In this context, a comprehensive study on the energy-water-solute nexus within 3D SGs is essential to optimize evaporation performance and hybrid functionalities.

To develop a more effective design strategy, numerical simulations — encompassing both macroscopic and microscopic-scale methods — can be used as powerful tools to investigate the dynamic processes of solar energy, heat, fluid and vapor within 3D SGs.[33] In recent years, numerical simulations have been extensively used to guide material design and optimize device configurations of 3D SGs, significantly enhancing evaporation performance while improving design and fabrication efficiency.[34-38] Specifically, numerical simulations provide essential support in uncovering the underlying mechanisms governing the balance of water, energy and environment (i.e., temperature, humidity, airflow and water wave) during photothermal conversion and reactions.[39-42] Macroscale simulating methods (i.e., COMSOL Multiphysics, Fluent, OpenFOAM and ANSYS) have proven instrumental in elucidating the intricate

correlations among gradient structures, thermal and mass transport, energy management, and the coupling of thermal and flow fields during solar evaporation.[43-46] These methods enable detailed representations of the dynamic distributions and transfers of energy, water, humidity and salt across both structural components and their surrounding environment, thereby providing invaluable insights into the devices' dimensions, operations and functions.[47-52] In addition, microscale simulating simulations (i.e., density functional theory, molecular dynamics and Monte Carlo methods) reveal kinetic characteristics and motion states of water molecules during solar evaporation, which remain inaccessible to experimental observation.[53-56]

Despite significant progress, current simulation techniques predominantly focus on individual 3D SGs. To enable efficient clean water production, 3D SGs must be integrated into system-level arrays, suitable for deployment in portable devices or solar distillation plants.[57] For large-scale implementation of 3D SG arrays, boosting photothermal conversion, solar evaporation and water collection within a compact area is of paramount importance.[58, 59] Beyond the optimization of individual SGs, the SG array's configuration — encompassing its shapes, sizes and inter-spacing — plays an even more critical role in enhancing evaporation performance. This gap — stemming from the complex, underexplored energy-water-solute interactions within 3D SG arrays — has constrained the development of system-level designs and scalable fabrication strategies for real-world, open-water applications. For future design, we believe that advancing numerical simulation and experimental evaluation methods to accurately design and predict the holistic evaporation performance of SG arrays and desalination systems represents a compelling research frontier, yet such a proof-of-concept remains elusive.

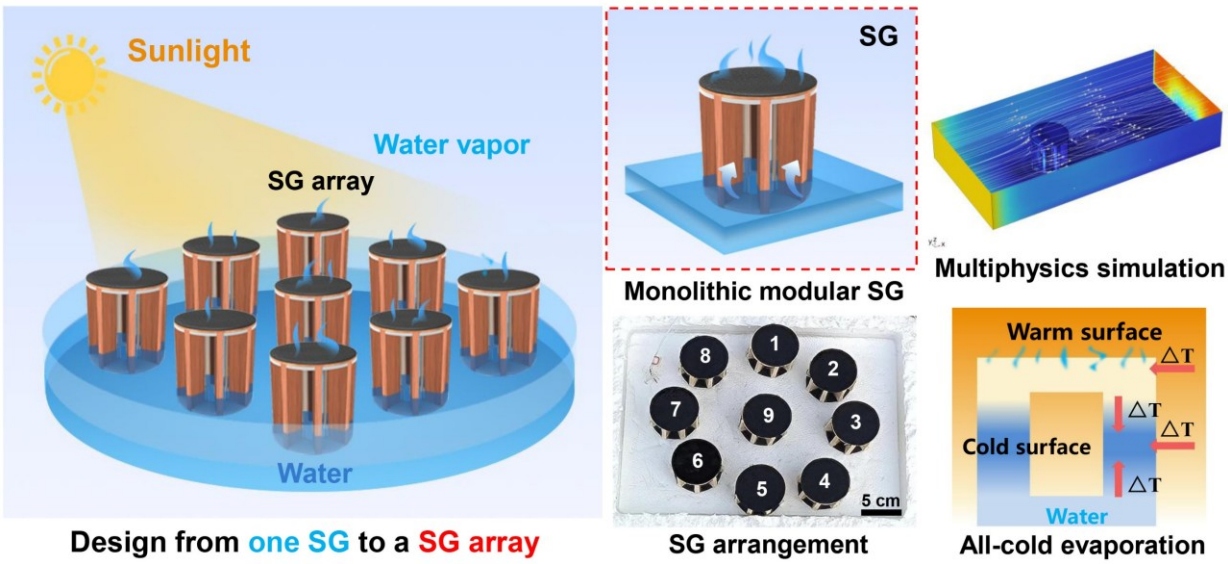

Figure 1. Schematic illustration and digital photographs of individual SGs and SG arrays optimized based on numerical simulation and experimental evaluation in this study.

In this contribution, a series of 3D SGs and their integrated SG arrays were fabricated and optimized to enhance solar-powered interfacial evaporation (**Figure 1**). Numerical simulations and experimental studies were synergistically conducted to optimize the structural components, device configurations of individual SGs and the arrangement of SG arrays. On one hand, COMSOL Multiphysics was employed to simulate the temperature, relative humidity (RH) and airflow distributions throughout SGs with varying numbers of fins, guiding the modulations of side fins and the arrangement of SG arrays. On the other hand, the experimental evaluation was performed under indoor, outdoor, windless and windy conditions. For individual SG units, the top surface efficiently converted solar energy into heat, facilitating solar evaporation, while excess thermal energy was transferred to the side fins to promote cold evaporation. Among five SGs, 8-Fin SG achieved the highest water evaporation rate of over 2.3 kg m^{-2} h^{-1} under 1 sun, and the value further increased to 4.8 kg m^{-2} h^{-1} under a moderate airflow of 2 m s^{-1}, placing it among the best-performing solar-powered SGs reported to date. Based on 8-Fin SG, the circular array with 12 cm spacing attained a water evaporation rate of 5.9 kg m^{-2} h^{-1} under natural sunlight. In this array, all structural components in each SG maintained temperatures

consistently lower than both air and water, enabling an "all-cold evaporation" mode with significant energy input from air and water into all SGs. This work highlights the significance of system-level array design in scaling up solar-powered interfacial evaporation for real-world applications, considering both theoretical and experimental perspectives.

RESULTS AND DISCUSSION

Fabrication and Characterization of SGs

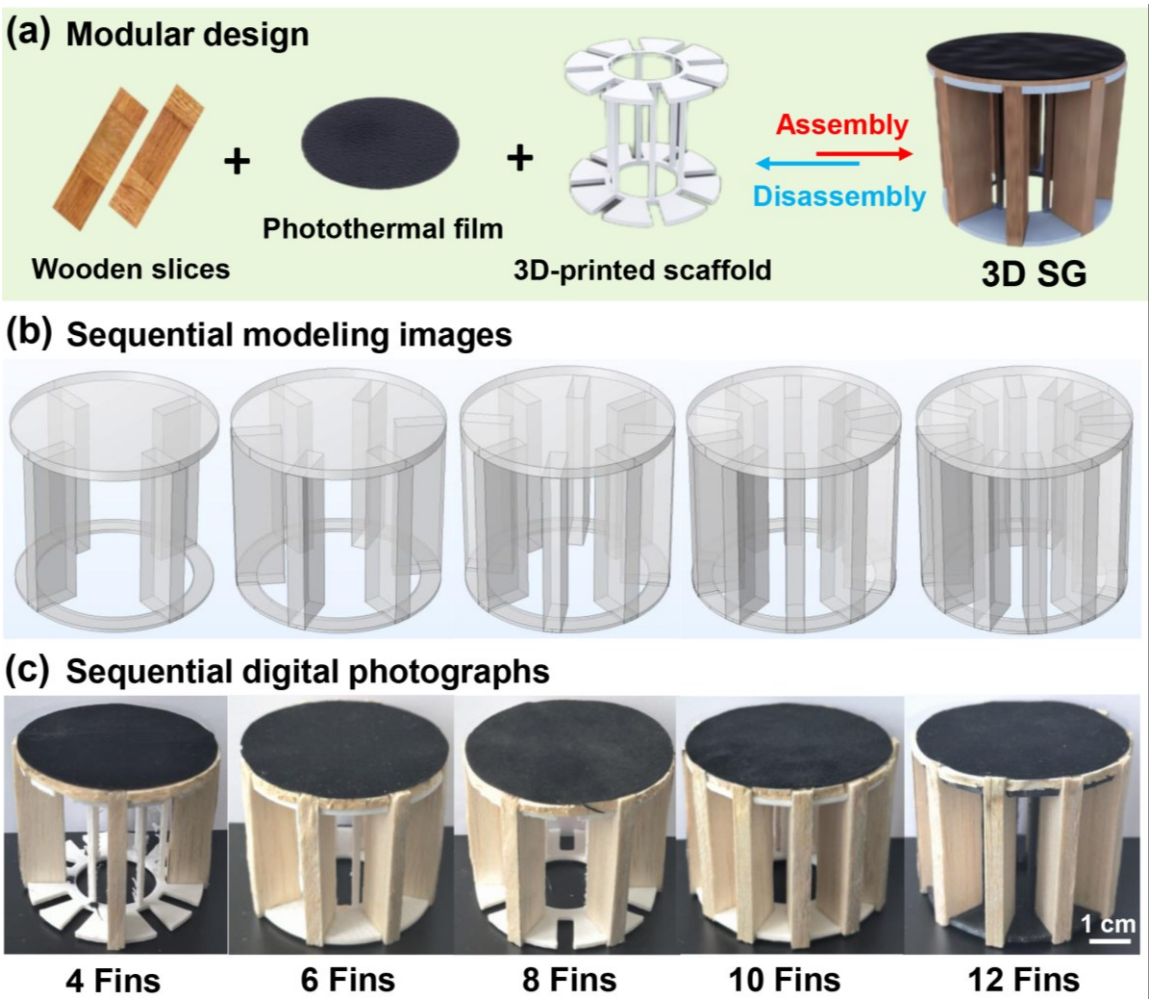

Figure 2. (a) Process flowchart for fabricating 3D SGs. (b) Sequential modeling images and (c) digital photographs of 3D SGs featuring heatsink-like structures with varying fin counts (from 4 to 12).

The fabrication process of 3D SG is depicted in **Figure 2a**. All fins (5.0 cm × 1.4 cm × 0.5 cm) within the heatsink-like structures were constructed from balsa wood, one of the lightest natural

woods available. This characteristic imparts excellent buoyancy, making balsa particularly suitable for SGs designed to float on water. Despite its lightweight nature, balsa boasts a high strength-to-weight ratio (0.12 $N \cdot m\ kg^{-1}$), which is advantageous for modeling purposes. In addition, the porous and oriented structure of balsa enhances its capacity for water diffusion and thermal insulation in specific directions.[60] Furthermore, a hydrophilic fiber mat, fabricated via an optimized electrospinning method using black polyurethane as the raw material, served as the photothermal layer atop SG. This fiber mat is not only strong and resistant to stretching and shrinking, but also more cost-effective than many natural fibers. A 3D scaffold was fabricated using extrusion-based 3D printing, which integrated the wooden slices as side fins and the photothermal film as the top surface. The fins directly contacted the photothermal layer, facilitating efficient water transport from the bottom to the top. This modular design allowed for easy disassembly of the fins from SGs.

The structural design and modeling of SGs are illustrated in **Figure 2b**. To modulate the number of fins, slots were incorporated into the 3D scaffold with rotational intervals of 90°, 60°, 45°, 36° and 30°. This configuration allowed for the assembly of five SGs with different fin counts: 4, 6, 8, 10, and 12 fins, respectively. Digital photographs of five SGs are presented in **Figure 2c**. All SG variants maintained a consistent height (5.3 cm) and diameter (6 cm) for comparative analysis, except for the systematic variations in the number of fins. The heatsink-like structures were designed to scale up evaporation areas of the SGs, enabling efficient convection to pass through their internal channels. The modular, disassemble design of SGs allowed for the modulation of side fins, facilitating the evaluation and optimization of evaporation performance, corroborated by simulation results.

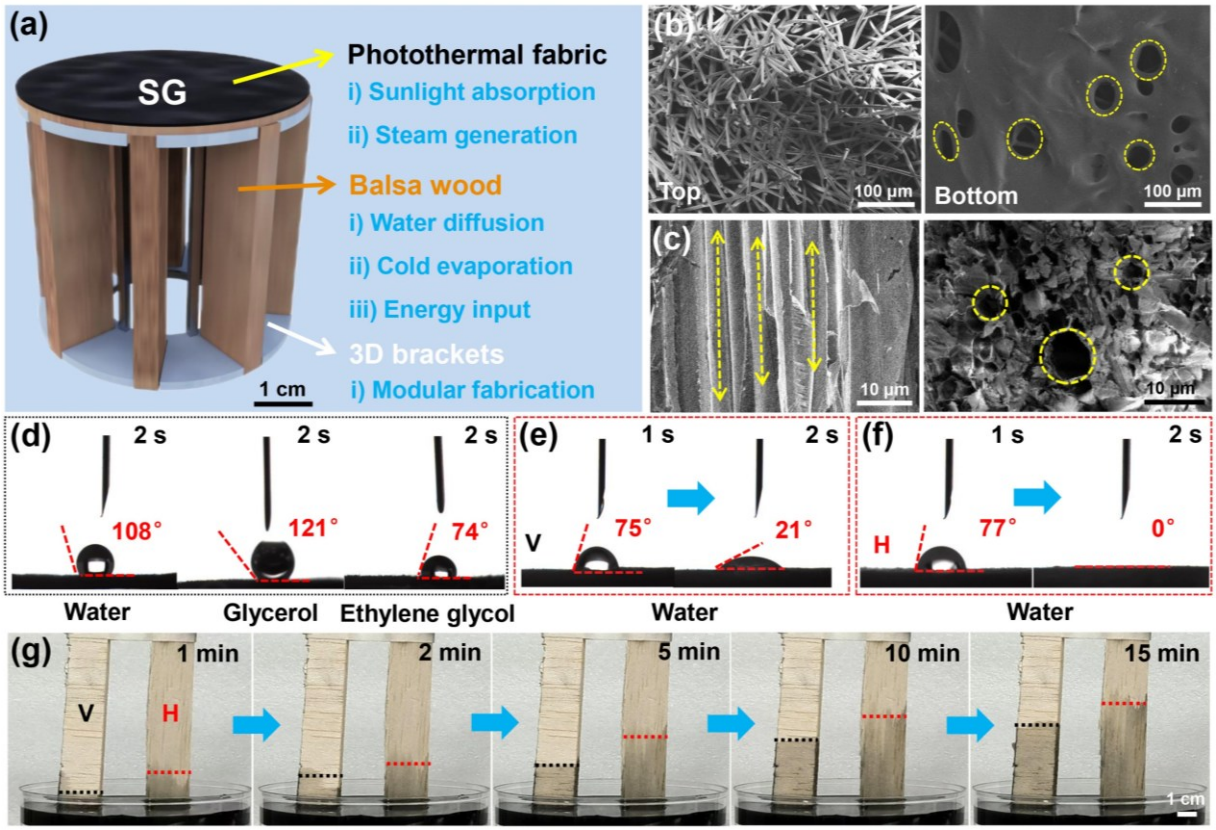

Figure 3. (a) Schematic illustration of structural components and their functions within SG. (b) SEM images of photothermal fabric (left: top view and right: bottom view). (c) Cross-sectional SEM images of balsa wood (left: longitudinal cross-section and right: transverse cross-section). (d) Contact angle measurements of photothermal fabric. Water contact angle measurements of (e) longitudinal and (f) transverse cross-sections of balsa wood. (g) Water diffusion characterization of balsa wood along the vertical (V) and horizontal (H) growth directions.

3D SG comprised three structural components: a photothermal fabric, detachable fins and a 3D-printed scaffold (**Figure 3a**). Given the critical role of balsa wood as a primary structural component in SGs, its structural stability was evaluated under extreme aqueous conditions, including highly acidic (pH = 1), alkaline (pH = 14) and saline (20 wt% NaCl) environments. After 14 days of immersion, the balsa wood sheets exhibited no dissolution or deformation, indicating their excellent structural stability for applications under harsh conditions (Figure S1). Notably, all SGs with varying numbers of fins sustained a 500 g load without collapse, exhibiting their structural stability and integrity (Figure S2). In addition, the photothermal

fabric afforded a broad absorptance of ~82.1% across the 250 − 2500 nm range, effectively absorbing the entire solar spectrum (Figure S3). Scanning electron microscope (SEM) imaging revealed a densely packed, bead-free nanofiber structure with an average fiber diameter of 44.3 nm (**Figure 3b** and Figure S4). Diameter distribution analysis was performed using Nano Measurer software on over 200 fibers across five distinct regions. An isotropic pore structure was observed in the underwater adhesive between the photothermal fabric and balsa wood. As a result, the photothermal fabric converted sunlight into thermal energy, heating the liquid water diffused from the balsa wood into the fabric and enabling the subsequent release of water vapor.

The balsa wood-based fins exhibited pronounced structural anisotropy as depicted via macro photography and SEM images (**Figure 3c** and Figure S5). The hierarchical porous structure of the balsa wood, formed by vessel and tracheid elements, spanned multiple length scales. The lumina of the vessels (microchannels) generally aligned along the longitudinal direction (the growth direction), where vessel and tracheid provided the large-size and small-size channels, respectively. This multiscale, anisotropic architecture facilitated efficient pathways for multiphase transport of water, nutrients and organic substances within the wood. Beyond water diffusion in SGs, heatsink-like structures with varied fin counts can increase the evaporation areas of SGs. Additional energy input pathways for evaporation could be created when the fin temperatures were lower than those of surrounding air and water. For individual SGs, this study evaluated the influences of fin count on their evaporation area, airflow, energy gain, and evaporation rates.

Previous reports have evidenced that hydrophilic porous surfaces can facilitat0.e the expulsion of water vapor from photothermal layers while preventing the accumulation of salt crystals, which is crucial for solar desalination.[61, 62] To assess this property, contact angle (CA) measurements were performed, revealing a hydrophilic surface (CA value: 108°) on the photothermal fabric (**Figure 3d**). In addition to water, the fabric exhibited high CA values when

tested with hydrophilic organic solvents such as glycerol and ethylene glycol, further validating its hydrophilic characteristics. CA measurements also reveal the hydrophilic nature of the cross-sections of balsa wood. Here, the cross-sectional surface perpendicular to the growth direction (vertical direction, denoted as V) showed a CA value of 75° at 1 s, which decreased to 21° after 2 s (**Figure 3e**). The cross-sectional surface parallel to the growth direction (horizontal direction, denoted as H) showed a slightly higher initial CA of 77° at 1 s, but it rapidly dropped to zero after 2 s (**Figure 3f**). Similarly, for organic solvents, the distinct CA responses to glycerol and ethylene glycol further suggest morphological variations between the V and H cross-sections of balsa wood (Figure S6).

To further investigate water transport properties, the water diffusion along the vertical (V) and horizontal (H) directions relative to the growth axis was characterized using an image sequence (**Figure. 3g**). In the vertical direction, water diffused to a distance of 4.3 cm within 15 min. A faster water diffusion was observed in the horizontal direction, where water reached a height of 5.5 cm in the same time frame. These results indicate superior water transport along the growth direction of balsa wood. Consequently, all fins were tailored from the balsa wood, with the wood's growth direction oriented perpendicular to the water surface.

Solar Evaporation Characterization of SGs at Indoor Conditions

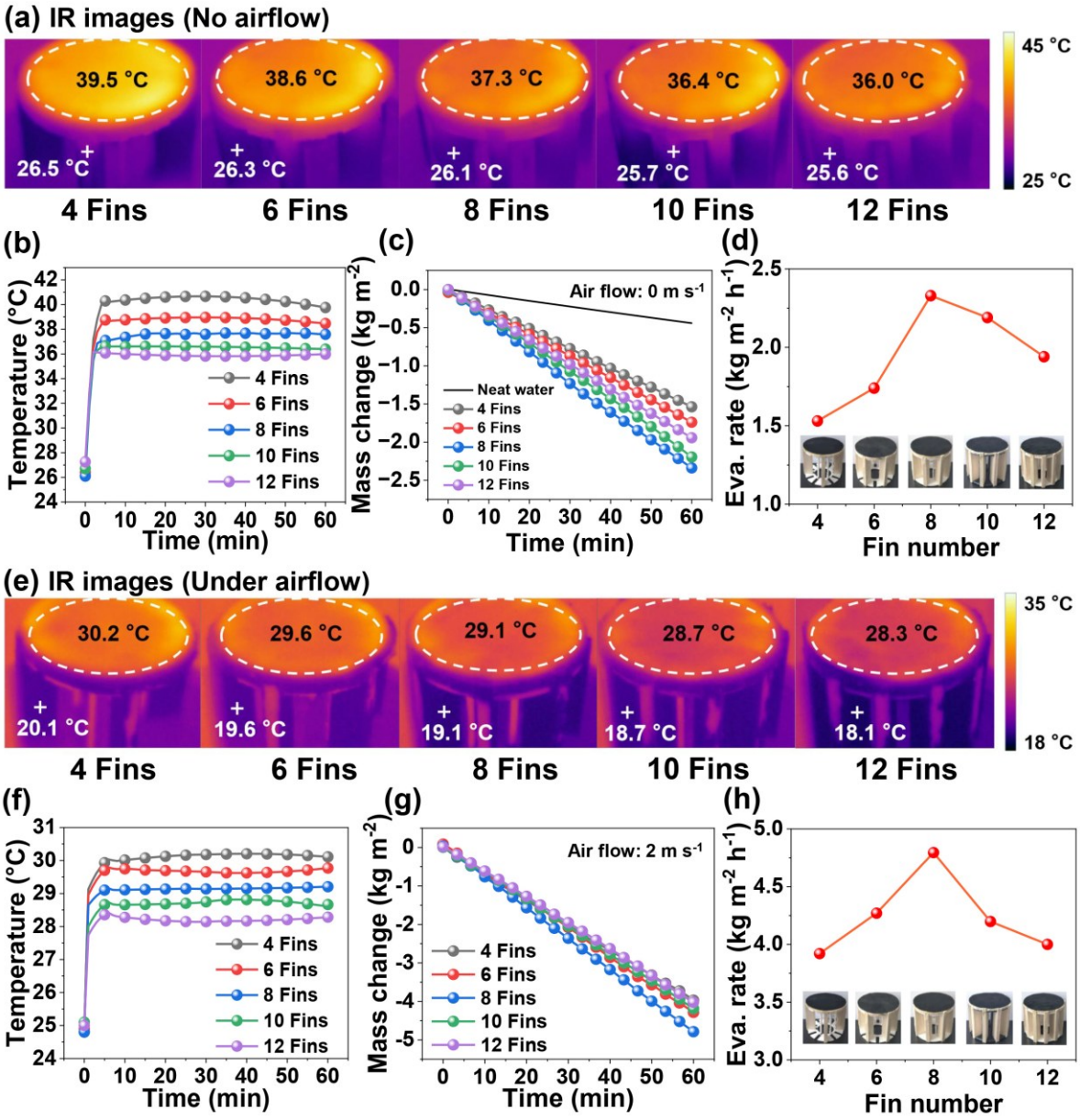

Figure 4. Solar evaporation characterization under windless and 1 sun conditions: (a) IR images at a steady state, (b) surface temperatures, (c) mass changes of water and (d) water evaporation rates of SGs over 60 min. Solar evaporation characterization under light breeze (2 m s^{-1}) and 1 sun conditions: (e) IR images at a steady state, (f) surface temperatures, (g) mass changes of water and (h) water evaporation rates of SGs over 60 min.

Indoor water evaporation measurements were performed under 1 sun (AM 1.5G, 100 mW cm^{-2}) at ~28 °C and ~50% RH. The bottom sides of all SGs were immersed in water, ensuring consistent height (5.1 cm) above the water surface for reliable comparisons. During the evaporation tests, solar illumination was exclusively directed onto the top surface of all SGs,

with the evaporation area defined as the projected surface area (diameter: 6 cm) to ensure consistent and reliable comparison across all SGs. To date, numerous 3D SGs with varying structures, dimensions and heights have been developed, while it is widely accepted that their projected surface areas are typically used as the standard metric for determining evaporation rates.[63] Tests were conducted under breezeless and breezy conditions, with air velocities set at 0 and 2 m s^{-1}, respectively. Temperature changes of top surfaces and side fins of SGs, water and air were monitored using an infrared (IR) camera and thermocouples. Under calm (windless) and 1 sun conditions, the surface temperatures of all SGs rapidly increased, reaching an equilibrant state in 5 min (**Figure 4a** and **Figure 4b**). SGs with fewer fins exhibited higher surface temperatures, while equilibrant temperatures decreased with increasing fin number. The surface temperatures of five SGs ranged from 36.0−39.5 °C, consistently exceeding the ambient temperature (~28 °C). On the other hand, the fin temperatures of all SGs ranged from 25.6−26.5 °C, remaining below the ambient temperature. These results highlight the presence of energy input pathways from the surrounding air to all SGs. Water evaporation rates were determined by measuring water mass loss over 60 min (**Figure 4c**). All SGs demonstrated significantly enhanced evaporation compared to neat water, as indicated by the sharp declines in water mass. The evaporation rates under calm and 1 sun conditions are summarized in **Figure 4d**. The rates were measured at 1.53, 1.74, 2.33, 2.19 and 1.94 kg m^{-2} h^{-1} for SGs with 4, 6, 8, 10 and 12 fins, respectively, with 8-Fin SG achieving the highest rate. Although increasing fin number expanded the evaporation area, it did not consistently enhance evaporation rates, as the rates gradually declined for 10- and 12-Fin SGs. These results reveal that solar evaporation can be effectively modulated by the fin number, with 8-Fin SG attaining the optimized performance among five SGs.

Airflow over water represents a critical environmental factor influencing interfacial water evaporation. Under light breeze (2 m s^{-1}) and 1 sun conditions, the surface temperatures of all

SGs rapidly increased, stabilizing in equilibrium within 5 min (**Figure 4e** and **Figure 4f**). For each SG, the surface temperatures under airflow were lower compared to those under calm conditions, attributable to enhanced convective heat loss. Interestingly, a consistent trend of decreasing equilibrium temperatures with an increasing number of fins was observed, mirroring the results obtained under calm conditions. Under enhanced convection, the surface temperatures of five SGs decreased compared to the calm condition, falling within the range of 28.3−30.2 °C, yet remaining higher than the ambient temperature (~28 °C). Notably, the side fins of all SGs exhibited significantly lower temperatures, ranging from 18.1−20.1 °C. Both windless and light breeze conditions highlight the mechanisms of energy transfer from the surrounding air, contributing to improved water evaporation. Furthermore, water evaporation rates were quantified by measuring water mass loss over 60 min (**Figure 4g**). Compared to calm conditions, airflow significantly enhanced water evaporation across all SGs. As summarized in **Figure 4h**, the evaporation rates under airflow and 1 sun were 3.92, 4.27, 4.80, 4.20 and 4.01 kg m^{-2} h^{-1} for SGs with 4, 6, 8, 10 and 12 fins, respectively. Notably, 8-Fin SG achieved the highest evaporation rate among five SGs, independent of convection. These results disclose that the heatsink-like structures in SGs enhance water evaporation by increasing evaporative surface area, promoting energy input from environment. The advantages of the structural modifications were closely linked to the optimization of side fins, underscoring the critical role of precise design in maximizing interfacial evaporation rates.

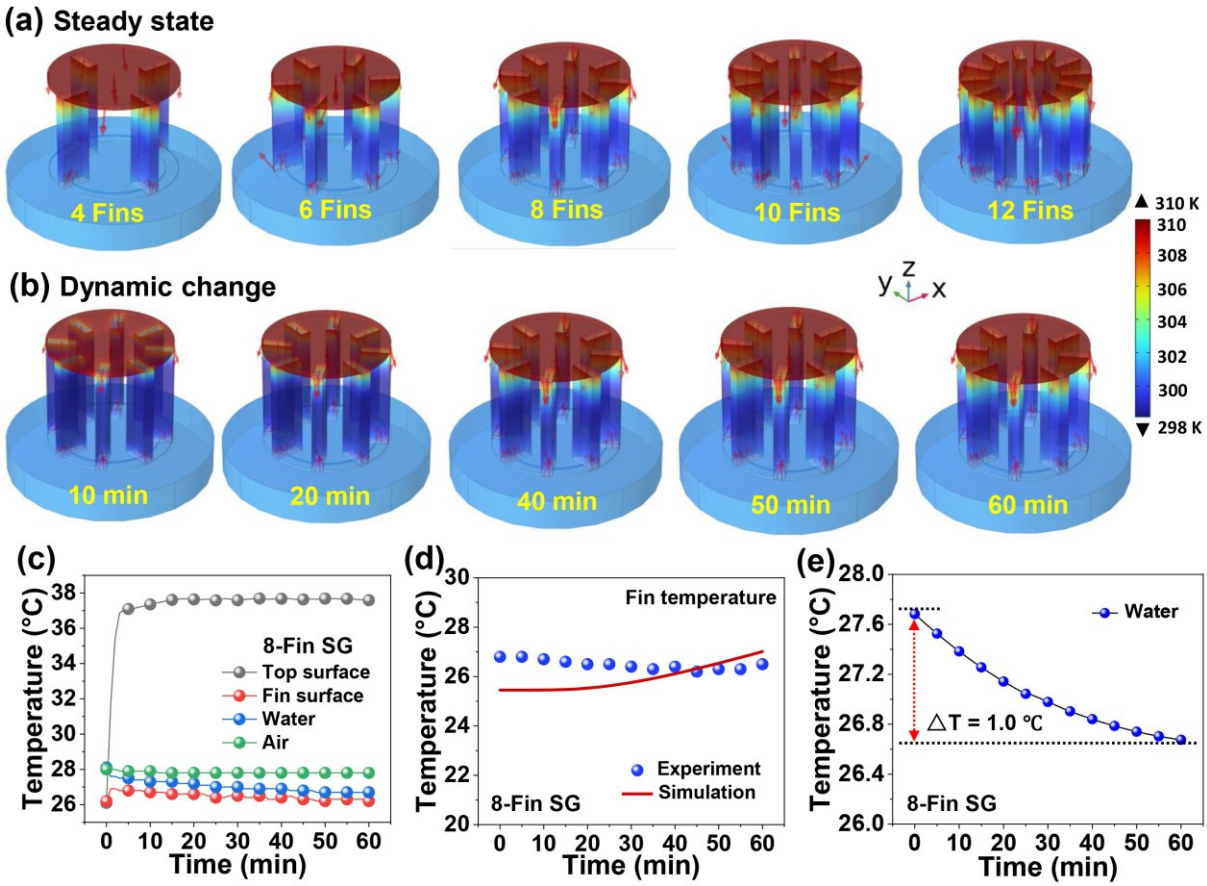

Figure 5. Temperature distribution characterization under windless and 1 sun conditions: (a) Temperature distributions of all SGs at a steady state. (b) Simulated temperature distributions of 8-Fin SG over 60 min. (c) Temperature changes of air, water and structural components within 8-Fin SG over 60 min. (d) Simulated and measured temperatures of fins within 8-Fin SG over 60 min. (e) Measured water temperature under 8-Fin SG over 60 min.

COMSOL Multiphysics was used to simulate the temperature distribution of SGs under windless and 1 sun conditions, aiming to validate the experimentally observed temperature variations of SGs and their surrounding environment during solar evaporation. The simulations employed the heat transfer module for solids and fluids, governed by the following equations 1 and 2,[64, 65]

$$\rho C_p \mathrm{u} \cdot \nabla T + \nabla \cdot q = Q + Q_{ted} \qquad (1)$$

$$q = -k \nabla T \qquad (2)$$

where Q represents the thermal flux (W m^{-3}), Q_{ted} denotes the additional thermal effect term

(W m^{-3}), q is the heat flux, k is the thermal conductivity, ρ corresponds to the density of water, C_P is the specific heat capacity of water at constant pressure, ρC_P is the effective volumetric heat capacity of water under constant pressure, u represents the fluid velocity field and ∇T is temperature gradient (K m^{-1}). 3D geometric models were constructed to match the actual dimensions of all SGs (Figure S7a). The fundamental material properties (i.e., density, temperature, thermal conductivity, and heat capacity at constant pressure) of the water-saturated photothermal mat and balsa wood, along with environmental parameters (i.e., solar intensity, RH and ambient and water temperatures) were determined based on experimental measurements. The model incorporated Multiphysics simulations, accounting for heat transfer within both solid and fluid domains. Physical boundary conditions were defined by considering the density, isobaric heat capacity, and thermal conductivities of the structural components and bulk water. The initial temperatures of all structural components were set to match the measured values obtained via IR imaging and thermocouples. A uniform heat flux of 100 mW cm^{-2} was applied to the top surfaces of all SGs as the solar energy input. The mesh of all SG models was generated with careful refinement of the boundaries of the structural components, air, and water (Figure S7b). In the steady state, the surface temperatures of five SGs ranged from 36.5 to 37.7 °C, which closely aligned with the experimentally measured values (**Figure 5a**). The temperature of the bulk water remained within a narrow range of 26.7−26.9 °C. For all SGs, it is noted that the temperatures of the side fins (26.2−26.5 °C) were lower than those of the top surfaces, surrounding air (~28 °C) and bulk water. The simulation reveals that SGs harvested energy both from the surrounding air and the bulk water during solar evaporation.

A transient simulation was performed using an 8-Fin SG model to analyze the dynamic temperature variations in water-saturated structural components, air and bulk water during solar evaporation. The temperature distribution was recorded at 1 min intervals over a 60 min duration. Sequential thermal images revealed that the temperatures of the water-saturated side

fins consistently remained lower than those of the surrounding air and bulk water throughout the 60 min solar evaporation (**Figure 5b** and Video S1).

To experimentally validate the simulated temperature profiles, temperature variations of 8-Fin SG and the surrounding environment were monitored using IR imaging and thermocouples under windless and 1 sun conditions (**Figure 5c**). The surface temperature of the 8-Fin SG exhibited a rapid increase, stabilizing at ~37.3 °C within 5 min. On the other hand, the temperatures of air and bulk water remained relatively stable at ~27.8 °C and ~26.7 °C, respectively. Notably, the lowest temperature was recorded at the side fins of SG, which retained a stable temperature of ~26.2 °C throughout the duration (**Figure 5d**). Sequential images in Figure 5b revealed a slight increase in temperature of the side fins from 25.5 °C to 26.8 °C, attributable to energy input from the surrounding environment. Although the measured temperatures of side fins were inevitably influenced by additional heat exchange pathways between SG and environment, the observed values remained consistent with the simulated temperature range. The gradual temperature decline in bulk water further corroborates the energy transfer from bulk water to the side fins of SG (**Figure 5e**). In developing the simulation model, we assumed that the SG absorbed heat exclusively from solar radiation, bulk water and the surrounding environment. The light intensity and air temperature were modeled as constant values, derived from measured experimental data. However, during actual experimental conditions, minor fluctuations in air temperature and movement may occur, potentially introducing slight discrepancies. Despite these variations, the results from both the simulation and experimental measurements exhibit minimal differences. Notably, both approaches consistently demonstrate that the fin temperature remained lower than that of the air and bulk water throughout the evaporation process. These results highlight the accuracy and consistency of both the simulated and measured temperature changes in 8-Fin SG, air and bulk water during solar evaporation.

To further clarify the contributions of hot and cold surfaces to evaporation, either the top surface or the side fins of the 8-Fin SG were selectively covered with tinfoil (Figure S8a). This approach enabled the isolation and evaluation of solar evaporation contributions from the hot surface (top) and the cold surface (fins). Solar evaporation was conducted over 60 min under windless and 1 sun conditions (Figure S8b and S8c). The evaporation rate of unmodified 8-Fin SG was as high as 2.33 kg m^{-2} h^{-1}. When only the top surface was exposed, the evaporation rate was 1.24 kg m^{-2} h^{-1}, while the evaporation rate from the fins alone was limited to 0.63 kg m^{-2} h^{-1}. The results reveal that evaporation from the hot surface dominated the total evaporation in 8-Fin SG, while the cold fins also contributed to water evaporation.

An analysis of the energy balance, energy losses, and energy gains was conducted based on the performance of 8-Fin SG during 1 h of solar evaporation (Section S12, Table S1 and Figure S9). Owing to the elevated surface temperature of SG compared to the surrounding air, the SG surface experienced inevitable radiation and convection losses. The total energy output comprised the energy expended in water evaporation (4.48 W), along with losses due to radiation (0.17 W) and convection (0.13 W), yielding a total output of 4.78 W. Conversely, the side fins, with temperatures lower than both the SG surface and the surrounding air, gained energy via radiation and convection from the surrounding air. Additionally, since the temperature of the side fins was lower than the water beneath SG — resulting in a 1 °C decrease in water temperature during solar evaporation — thermal conduction from the water further contributed to energy gain in the fins. The total energy input included solar irradiation (2.58 W), along with environmental energy inputs through radiation (0.14 W), convection (0.10 W) and conduction (0.20 W), summing to a total of 3.02 W. These results quantify the energy losses and gains within the 8-Fin SG, suggesting that a portion of the energy loss can be recaptured through the energy gain from the surrounding environment during solar evaporation.

Solar desalination of 8-Fin SG was evaluated using different brine solutions under windless and

1 sun conditions (Figure S10a and S10b). The evaporation rate in a 1% NaCl solution reached 1.93 kg m^{-2} h^{-1} over 1 h, while an evaporation rate of 1.71 kg m^{-2} h^{-1} was achieved in seawater over the same duration. Both values are comparable to the evaporation rate of 2.33 kg m^{-2} h^{-1} obtained in freshwater. Furthermore, cyclic solar desalination tests were conducted, where the 8-Fin SG was subjected to alternating 12 h illumination under 1 sun and 12 h dark conditions, simulating day−night cycles (Figure S11). Over 15 cycles, an average evaporation rate of 1.68 kg m^{-2} h^{-1} was retained. These results highlight the performance and stability of 8-Fin SE for solar desalination in saline environments.

Solar Evaporation Simulations of SGs

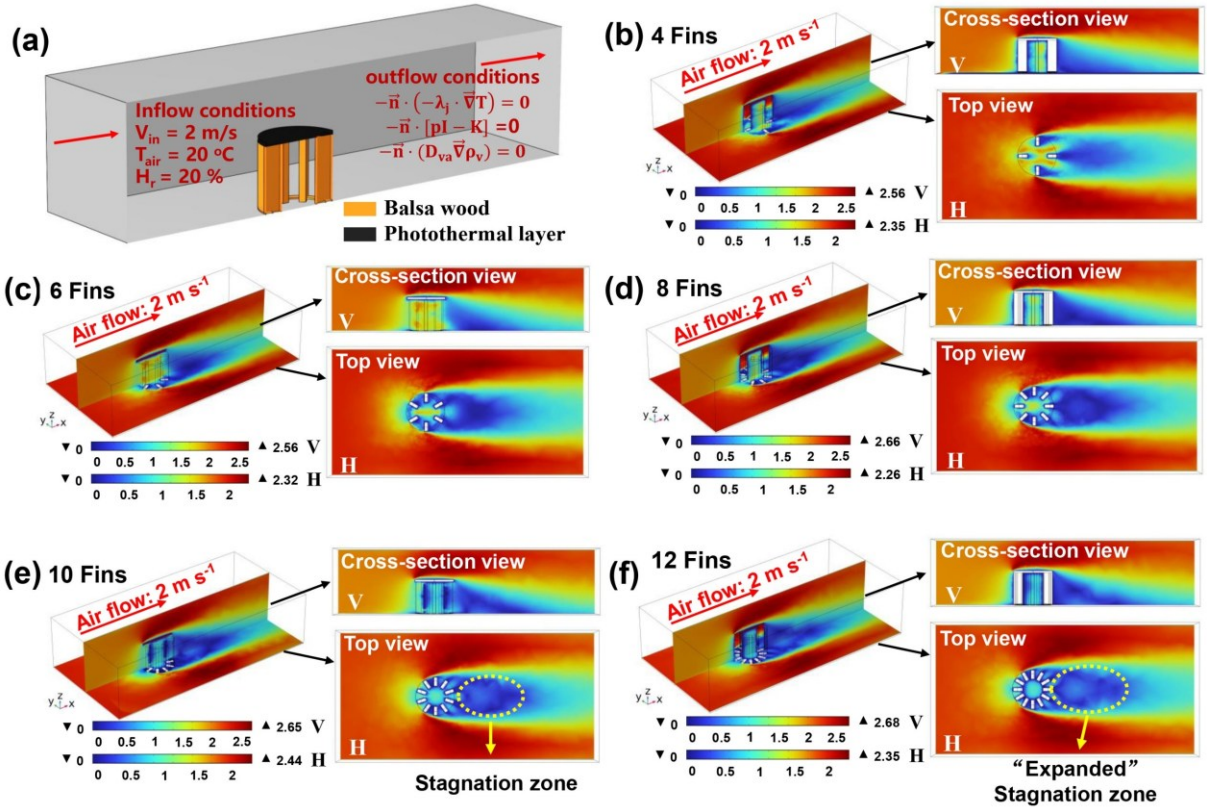

Figure 6. (a) Boundary condition settings for convection simulations of SGs. (b−f) Airflow distributions across five SGs with varying fin number under 1 sun and a light breeze (air velocity: 2 m s^{-1}).

Solar evaporation characterization demonstrates that convection flow significantly enhanced the water evaporation rates of SGs when the number of their side fins was fewer than eight.

However, experimental studies did not fully explain the observed phenomenon: the water evaporation rates of SGs reached their highest value when eight fins were incorporated, and decline gradually as the number of side fins exceeded eight. To address this question, COMSOL Multiphysics was employed to simulate the air velocity and RH distribution throughout SGs, and the changes of their surrounding environment during solar evaporation. A Multiphysics approach was applied to the model, incorporating air turbulence, heat transfer across multiple domains, and water vapor transport in the surrounding air. Boundary conditions for each SG were defined on the blue surfaces, representing the boundaries for convective flow inlet and outlet, vapor outlet and evaporation flux (Figure S12). The simulation of air velocity distribution can be expressed using the following equations 3−5,[66, 67]

$$\rho\frac{\partial \mathrm{u}}{\partial \mathrm{t}}+\rho(\mathrm{u}\cdot\nabla)\mathrm{u}=\nabla\cdot[-\mathrm{p}I+K] \tag{3}$$

$$\frac{\partial \rho}{d\mathrm{t}}+\nabla\cdot(\rho\mathrm{u})=0 \tag{4}$$

$$K=(\mu+\mu_T)\left(\nabla\mathrm{u}+(\nabla\mathrm{u})^T\right)-\frac{2}{3}(\mu+\mu_T)(\nabla\cdot\mathrm{u})I \tag{5}$$

where u is the velocity field, ρ is the density of the fluid, p is the pressure, I is the constitutive relation coefficient, K is the fluid viscosity, μ is denoted as the dynamic viscosity, μ_T is turbulent viscosity; ∇ is gradient operator; $\nabla\cdot$ is divergence operator, (∇u) is velocity gradient tensor, $(\nabla u)^T$ is transpose of the velocity gradient tensor. 3D geometric models were constructed to accurately reflect the dimensions of all SGs, with an outer cuboid (40×20×10 cm^3) representing the surrounding air volume (**Figure 6a** and Figure S13a). The critical properties (i.e., density, porosity, thermal conductivity, and heat capacity) were specified for each structural component, while environment parameters (i.e., solar intensity and ambient temperature) were based on experimentally measured values. The meshes were generated, with specific refinement applied to the interfaces between all SGs and the surrounding air (Figure S13b). Two air velocity

conditions were considered: one representing a negligible value (10^{-16} m s^{-1}) to simulate a calm condition, and the other corresponding to a light breeze (2 m s^{-1}). Upon reaching a steady state under a windless condition (air velocity: 10^{-16} m s^{-1}), the air velocity distribution around five SGs and the surrounding environment are depicted in Figure S14. The images show negligible variation in air velocity around SGs with different fin configurations. Notably, the airflow within all SGs was close to zero, indicating the absence of convection passing through the side fins of SGs. As the air velocity increased to 2.0 m s^{-1}, the airflow passed over the top surfaces and lateral fins of all SGs (**Figure 6b−f**). For each SG, a distinct region of reduced velocity, referred to as the "stagnation zone" was observed, as the airflow passed through the SG. The size of this stagnation zone was smallest in the 4-Fin SG, and progressively enlarged with the addition of lateral fins. Notably, 12-Fin SG exhibited the largest stagnation zone, where the air velocity was significantly reduced within the outlet area. This result indicates that airflow can pass through the lateral fins of SGs, yet an excessive number of fins obstructed the smooth pathways of airflow through SGs, leading to increased flow resistance.

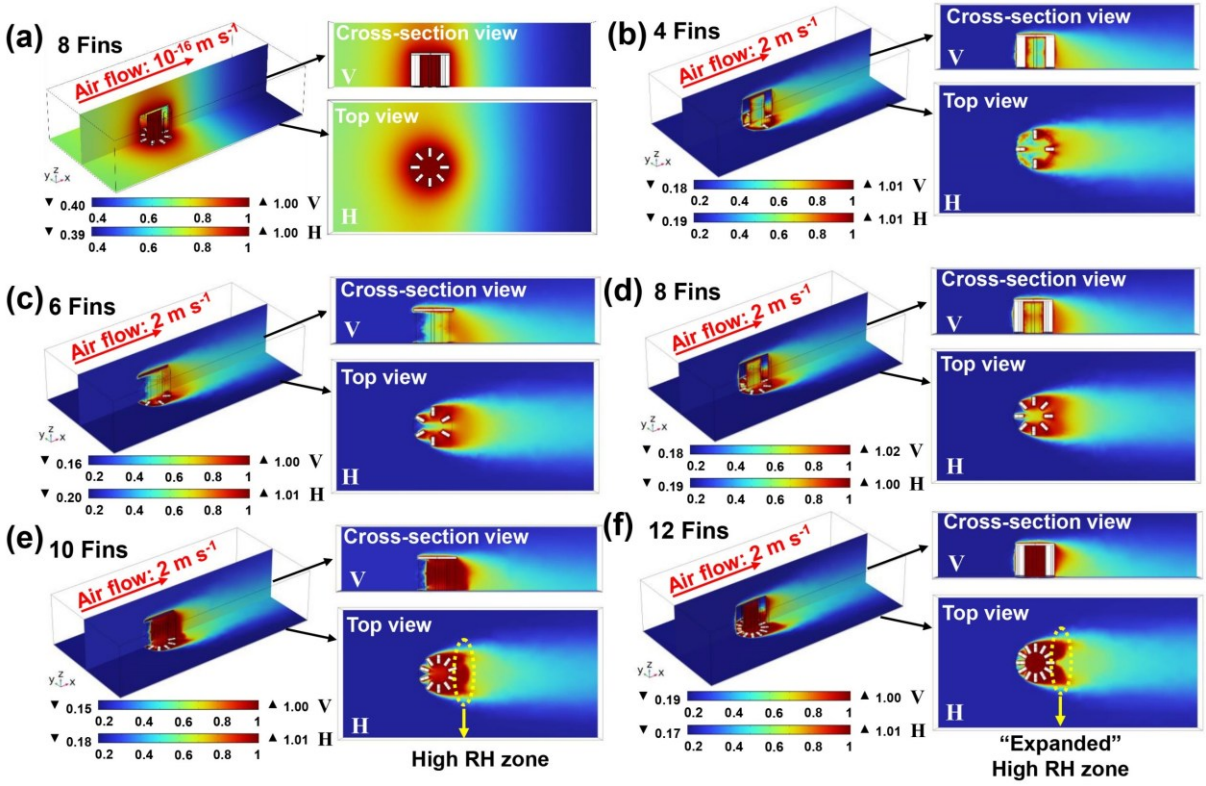

Figure 7. (a) RH distributions of 8-Fin SG under 1 sun and windless conditions (air velocity: 10^{-16} m s^{-1}). (b–f) RH distributions of SGs with varying fin number under 1 sun and a light breeze (air velocity: 2 m s^{-1}).

Subsequent simulations of heat transfer and moisture transport were conducted based on the steady-state airflow (fluid field) to determine the RH distributions around SGs. The simulation of RH distribution can be expressed using the following equations 6–8,[66, 67]

$$M_v \mathrm{u} \cdot \nabla C_v + \nabla \cdot g = G \quad (6)$$

$$g = -M_v D \nabla C_v \quad (7)$$

$$C_v = \phi C_{sat} \quad (8)$$

where M_v is the molar mass of vapor, u is the air velocity field, C_v is the vapor concentration, g is the moisture flux, G is the moisture source, D is diffusion coefficient, Φ corresponds to RH and C_{sat} represent the vapor saturation concentration, respectively. To simulate evaporation under windless conditions, a negligible air velocity of 10^{-16} m s^{-1} was applied. Once a steady state was reached, the simulated RH distributions around SGs are presented in **Figure 7a** and Figure S15. Similar to the airflow patterns, all SGs exhibited nearly identical RH distributions under the windless condition. Evaporated moisture accumulated distinctly around all SGs, with the regions of low air velocity inside SGs displaying high RH levels. On the other hand, the presence of convection (air velocity: 2.0 m s^{-1}) effectively removed the evaporated moisture, preventing the accumulation of water vapor around SGs (**Figure 7b–f**). Notably, an increase in the number of fins and the corresponding expansion of the stagnation zone for airflow led to a gradual enlargement of high RH regions around SGs, particularly in the outlet area of water vapor. Compared to SGs with fewer fins, the high RH regions of 10-Fin and 12-Fin SGs more pronounced, with RH values approaching 100%. The simulated RH distributions closely matched the airflow patterns.

In brief, our heatsink-inspired SG design used lateral fins to enhance solar-powered evaporation by expanding surface areas and improving thermal distribution. Notably, the indoor experimental results indicate a non-monotonic performance relationship with fin number (4−12 fins), with the 8-Fin configuration achieving peak evaporation rates. Furthermore, COMSOL simulations demonstrate that excessive fins (10 and 12) created pronounced airflow stagnation zones and localized high-humidity regions (RH: ∼100%) within SGs, significantly impeding vapor diffusion. These results establish that optimal fin number critically balanced surface area expansion with humidity and airflow management, thereby maximizing the solar-powered evaporation performance.

Solar Evaporation Simulation of SG Arrays

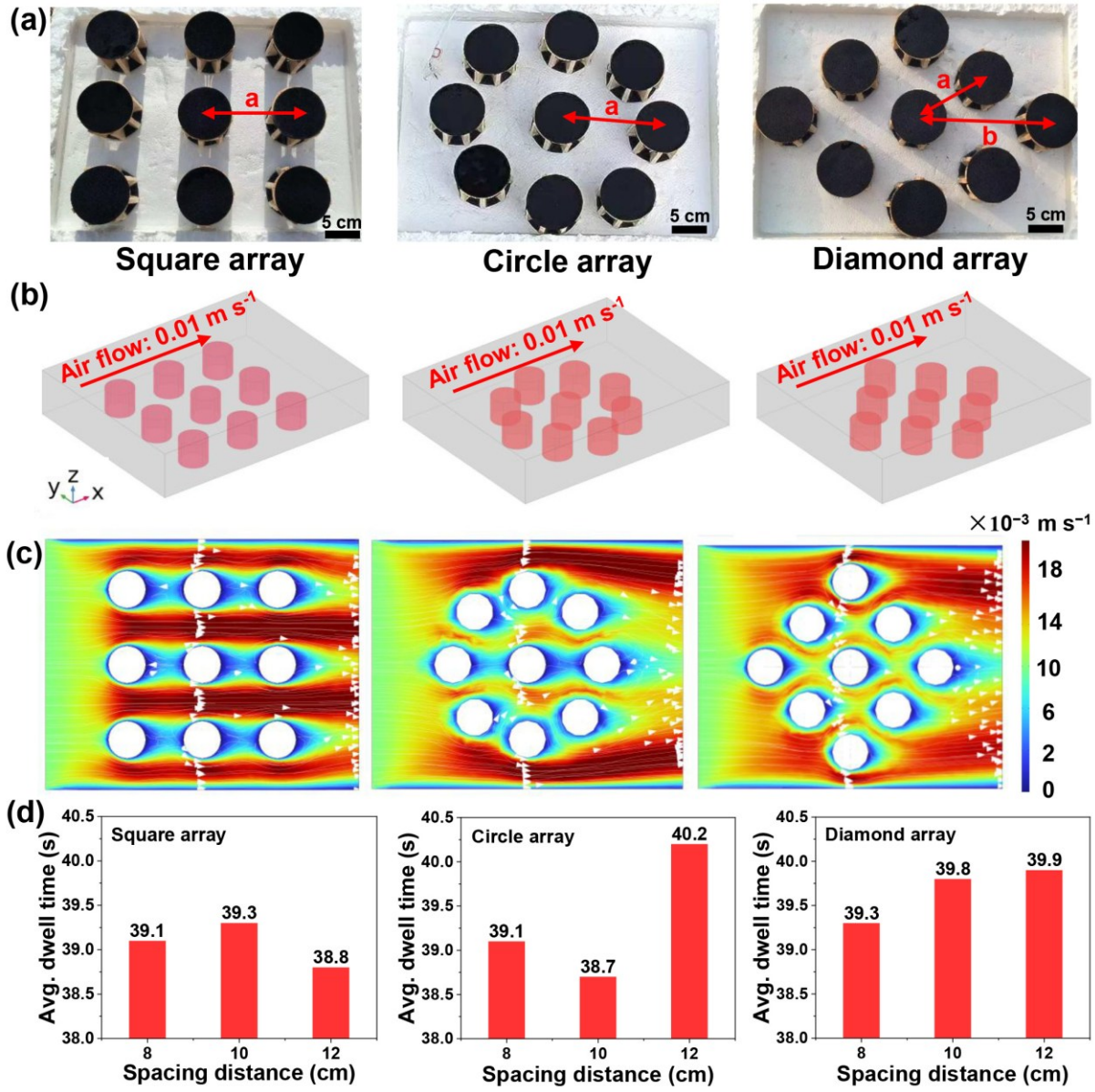

Figure 8. (a) Digital photographs and (b) geometric modeling of square, circular and diamond arrays based on 8-Fin SGs. Simulations of (c) airflow distribution and (d) average dwell time of air particles across square, circular and diamond arrays under a light breeze (air velocity: 0.01 m s^{-1}).

Portable instruments and large-scale water plants designed for future solar distillation could be based on strategically arranged high-performing SGs for boosting interfacial evaporation and clean water production. In addition to evaluating the airflow, RH distribution, and evaporation performance of individual SGs, comprehensive simulations were conducted to optimize SG array configurations for large-scale and outdoor applications. 8-Fin SG was selected as the

building block for all arrays, due to its superior evaporation rate compared to other SGs. Arrays in square, circular and diamond shapes were fabricated, with each array comprising nine 8-Fin SGs (**Figure 8a**). The inter-SG spacing for the square, circular, and diamond arrays were defined as 'a', 'a', and '(a + b)/2', respectively. For optimization, the spacing distances in each array were varied at 8, 10 and 12 cm, resulting in nine SG arrays for simulation. In previous outdoor experiments, natural convection plays a role in sweeping water vapor away from individual SGs and the arrays, with the removal rate controlled by the array consignations. To elucidate this process, the vertical movement and dwell time distribution of air particles passing through these SGs arrays were simulated. The varying array arrangements and spacing distances resulted in differences in the dwell time of air particles, as they traversed the SG arrays. The air velocity distribution field formed the foundational basis for the dwell time simulation. Specifically, air particles were subjected to dwell time distribution calculations within this velocity field to determine their dynamics throughout SG arrays.

All SG arrays were integrated with COMSOL Multiphysics, accounting for air turbulence, fluid flow and particle tracking. The dynamics of air particle movement and dwell time can be described by the following equations 9 and 10,[68]

$$\frac{d^2q}{dt^2} = \frac{\rho_p - \rho}{\rho_p} g + \frac{1}{\tau_p}(u - v) \qquad (9)$$

$$v = \frac{\tau_p}{m_p} F_{other} + u \qquad (10)$$

where ρ_p is the density of the air particle, ρ is the density of the surrounding fluid, g is the acceleration due to gravity; u is the velocity of the surrounding fluid, v is the velocity of the particle ($v \equiv dq/dt$), τ_p is the lagrangian time scale, F_{other} is the sum of all the forces except for the trailing force, and m_p is mass of the air particle. 3D geometric models for nine arrays were constructed to accurately represent the dimensions of individual SGs (diameter: 6 cm and height:

5.3 cm), with an enclosing cuboid (50×40×10 cm^3) designed to simulate the surrounding air volume (**Figure 8b**). The aerodynamic diameter of the air particles was defined as 5.0×10^{-7} m, with a particle density of 1.204 kg m^{-3}. Physical boundary conditions were established to specify the entrance and outlet for air particles. Meshes were generated for all nine arrays, with particular refinement applied to the interfaces between each SG and the surrounding air (Figure S16). The simulation included 3000 air particles with an initial velocity of 0.01 m s^{-1}, and the dwell time of air particles within different SG arrays were recorded (Figure S17 and Video S2). During the simulation of the dwell time of air particles, the initial velocity of the particles should be defined within an appropriate range to enable accurate observation of their movement. As a result, the initial velocity was adjusted to 0.01 m s^{-1}, allowing for a more detailed and precise analysis of particle movement and distribution. In addition, the airflow direction was consistently defined as parallel to the water surface, ensuring uniform passage through the SG arrays.

The convection distributions across the nine arrays were presented (**Figure 8c** and Figure S18, S19 and S20). For each array, the transient pathways of air particles were analyzed, indicating that the dwell time followed a normal distribution. It is hypothesized that air particles can carry water molecules away from the SGs and the array during evaporation. In these arrays, where all SGs were identical, a longer dwell time of air particles within the array increased the likelihood of interaction with water vapor generated by the SGs. Consequently, SG arrays with longer dwell times of air particle could present higher evaporation rates. The average dwell times for the nine arrays are summarized in **Figure 8d**. For square arrays, the array spacing with 10 cm SGs resulted in the longest dwell time of 39.3 s. For circular arrays, the longest dwell time of 40.2 s was observed with a 12 cm SG spacing, while the diamond arrays showed a maximum dwell time of 39.9 s, also at a 12 cm SG spacing. These results indicate that the average dwell time of air particles can serve as a reliable metric for assessing the evaporation

performance of SG arrays. The validity of the simulation results was corroborated through outdoor experiments with SG arrays, as detailed in the following section.

Outdoor Characterization of SG Arrays

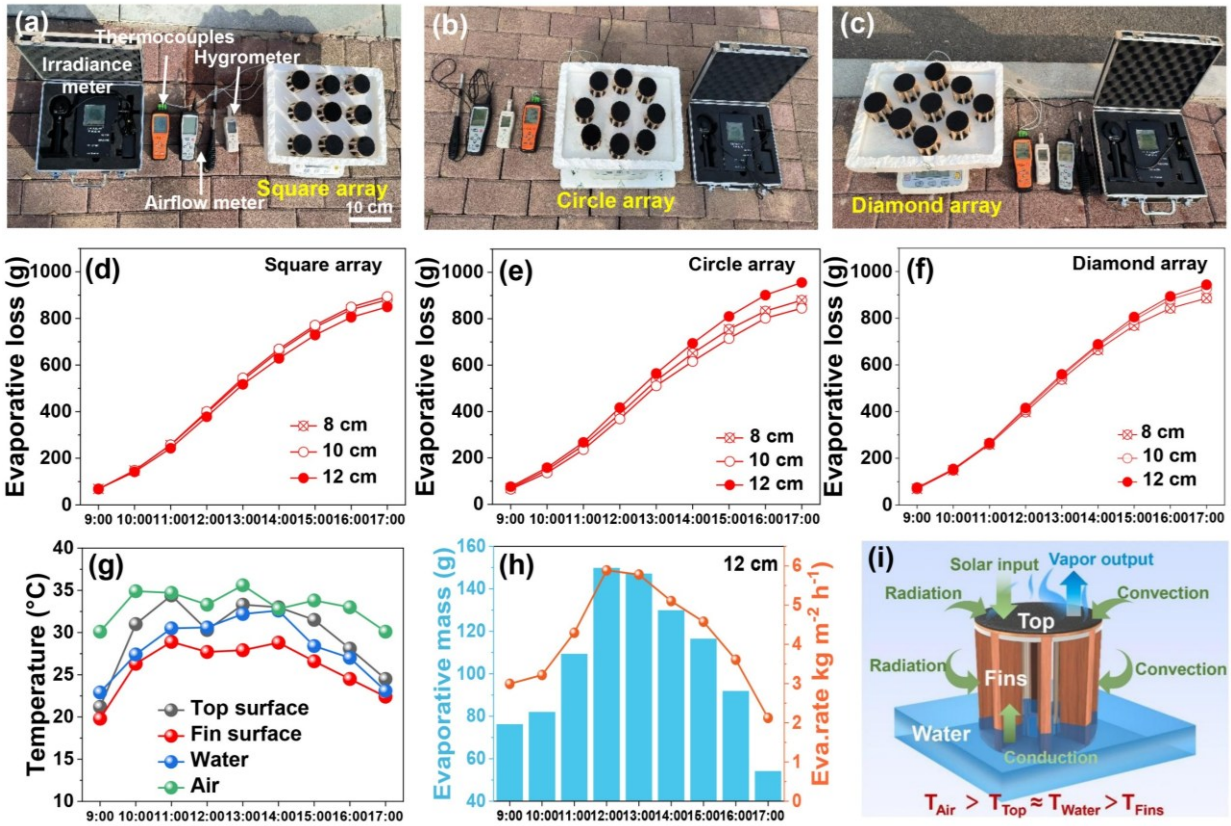

Figure 9. Digital photographs of the experimental setup for outdoor characterization of (a) square, (b) circular and (c) diamond SG arrays under a real sky. Summary of cumulative water loss during evaporation in (d) square, (e) circular and (f) diamond arrays. Summary of (g) temperature distribution and (h) water evaporation of the circular array (spacing distance: 12 cm). (i) Energy flow pathways of 8-Fin SG in an "all-cold evaporation" array.

To evaluate the evaporation performance of SG arrays under real-world conditions, outdoor experiments were conducted during the daytime (9:00−17:00) in June, Qingdao, China. 8-Fin SG was selected as the building block for all arrays, in good agreement with the simulation parameters. Nine arrays, configured in square, circular, and diamond SG arrangements with varying spacings (8, 10 and 12 cm) were placed on water bodies, and the mass changes of water

were recorded over time (**Figure 9a−c**). All individual SGs were fixed into designated holes on plastic foams, with both the SGs and holes sharing the same diameter. This configuration ensured that the surrounding water body was covered by the foam, effectively eliminating the influence of evaporation from the exposed water surface. Filtered natural seawater was employed as the water source for the outdoor experiments. The position of the sun was tracked using azimuth and elevation angles. On a sunny and breezy day, the solar elevation angle was 30° at 9:00, peaked at 72° around 13:00, and dropped below 30° by 18:00 (Figure S21a). Critical environmental parameters, including solar intensity, air velocity and RH were continuously monitored (Figure S21b). In the daytime, solar intensity ranged from 60−102 W m^{-2}, while air velocity varied between 0.3 and 2.2 m s^{-1}. The summer air remained dry, with RH values between 18% and 33%.

The total water losses of nine SG arrays were evaluated over 8 h, and resulting water mass changes are summarized in Figure S22, S24 and S26. For the square arrays with spacings of 8, 10 and 12 cm, the total water losses were 879.9, 893.8 and 849.5 g, respectively (**Figure 9d**). For the circular arrays, these values were 879.5, 845.1 and 955.8 g, respectively (**Figure 9e**). The diamond arrays with 8, 10 and 12 cm spacings showed total water losses of 885.5, 926.7 and 940.9 g, respectively (**Figure 9f**). Notably, the measured water losses of the SG arrays were in good agreement with the simulated dwell times of air particles, with the highest evaporation in each group corresponding to the arrays exhibiting the longest dwell times of air particles. Among the nine arrays, the circular array with a 12 cm spacing attained the highest water evaporation over 8 h, highlighting its superior evaporation performance.

Within this circular array, the temperature changes of air, water, SG surfaces and fins were monitored for individual 8-Fin SG units over the same period (**Figure 9g**). Consistent with single-unit tests, all SG fins demonstrated the lowest temperatures, remaining lower than both air and water, providing additional evidence of energy harvesting from the surrounding

environment. Notably, the surface temperature of each SG decreased below the ambient air temperature during evaporation, demonstrating the complete elimination of radiation and convection losses in the SG array. The observed "all-cold evaporation" phenomenon, characterized by zero thermal energy loss, aligns with recent reports in the literature.[69] In such systems, surface reflection from photothermal layers emerges as the dominant energy loss mechanism, while convective and radiative losses are effectively eliminated through sub-ambient operation. The water evaporation rates of all SG arrays in the daytime are summarized in Figure S22−S26. Among the nine SG arrays, the circular array with a 12 cm spacing achieved the highest evaporation rate. The highest evaporation (149.7 g) of this SG array occurred at noon (12:00 − 13:00), achieving an impressive evaporation rate of 5.89 kg m^{-2} h^{-1} under real-sky conditions (**Figure 9h**). In contrast, the evaporation rate of neat water during the same period was only 0.64 kg m^{-2} h^{-1} (Figure S28). The outdoor measurements based on a variety of SG arrays corroborate the simulation results, demonstrating that the dwell time of air particles is a reliable metric for assessing the evaporation performance of SG arrays.

An energy balance analysis was conducted on a circular array with 12 cm spacing, specifically focusing on each 8-Fin SG during a 1 h of solar evaporation at noon (12:00 − 13:00). The energy nexus and reversed energy flow pathways of SG are illustrated in **Figure 9i**. The solar energy input was estimated to be 1.29 W for each SG. Given that the temperatures of both the surface and side fins were lower than the surrounding air, these fins absorbed energy from air through radiation and convection, contributing a remarkable energy gain equivalent to 128.7% (1.67 W) of the incident solar radiation. Additional energy input from the water beneath each SG further enhanced the overall energy gain of the SG array. Assuming that 100% of the incident solar energy was used for evaporation, the SG array demonstrated an exceptional energy efficiency of ~401.0%, driven by the supplementary energy input from the environment (air and water) in conjunction with the incident sunlight. The energy nexus for each SG within this array can

be expressed by equation 11,[7]

$$E_{evaporation} = \alpha E_{in} + \left|E_{conduction}\right| + \left|E_{convection-1}\right| + \left|E_{radiation-1}\right| + \left|E_{convection-2}\right| + \left|E_{radiation-2}\right| \quad (11)$$

where E_{in} is the incident solar energy, α denotes the light absorption coefficient, $E_{convection\text{-}1}$ and $E_{radiation\text{-}1}$ represent the convection and radiation losses from photothermal surfaces (i.e., black mats), respectively. $E_{convection\text{-}2}$ and $E_{radiation\text{-}2}$ represent the convection and radiation energy gains at cold evaporation surfaces (i.e., fins) from environmental sources (air and water). This formulation reveals that, rational design of 3D SGs and SG arrays can achieve a fundamental reversal of conventional energy flow through all-cold evaporation. Instead of dissipating thermal energy to the environment, each SG in the array actively harvested thermal energy from both bulk water and surrounding air, enabling complete elimination of thermal losses, additional energy input from the environment, and dramatic enhancement of evaporation performance.

A single-stage, portable water production device was fabricated, incorporating the optimized 8-Fin SG array with a circular configuration and a 12 cm spacing between units (Figure S29). Long-term solar distillation tests were conducted by deploying the device under real sky for 15 days. The device demonstrated a daily water collection capacity of up to 269.6 g (10.6 kg m^{-2} d^{-1}) under sunny conditions and 134.1 g (5.3 kg m^{-2} d^{-1}) under cloudy conditions (Figure S30). Water quality was characterized via an inductively coupled plasma mass spectrometry (ICP-MS). After solar distillation, the concentrations of key elements (Na, Mg, K, and Ca) were well below WHO drinking-water quality standards (Figure S31). The results highlighted the effectiveness of solar-powered SG arrays in producing safe, potable water. Beyond solar evaporation, synergistic clean water collection has received comparatively less attention. Conventional solar stills often suffer from limited clean water collection rates due to inefficient air cooling and condensation within sealed chambers. To address this, innovative single- and multi-stage water purification systems have emerged, leveraging separated evaporation and condensation pathways, directional vapor flow, passive cooling enhanced by convection and

water, and radiative cooling to the deep sky.[70]

CONCLUSION

In summary, a series of 3D SGs was successfully fabricated and demonstrated for high-performance solar-powered interfacial evaporation, supported by a combination of numerical simulations and experimental validation. This capability was validated not only for individual devices but also for integrated SG arrays. The distinctive advantages of combining numerical simulations and experimental studies in this work are summarized as follows: (i) Rational design of heatsink-like SGs: 3D SGs consisted of a top photothermal surface seamlessly integrated with heatsink-like side fins, forming a monolithic, modular and disassemble structure. Upon solar irradiation, the top surface efficiently converted solar energy into heat, driving solar evaporation. Simultaneously, excess thermal energy was channeled into the side fins with expended evaporation areas, thereby enhancing cold evaporation. (ii) Optimization of SG configurations via simulation and experimental studies: COMSOL Multiphysics was employed to simulate the temperature, RH and airflow distributions throughout SGs with varying numbers of fins, guiding the modulations of side fins within SGs. The experimental results confirmed the numerical simulations under both calm and light breeze conditions. Among five SGs, 8-Fin SG attained the highest water evaporation rate of over 2.3 kg m^{-2} h^{-1} under 1 sun, and the value further increased to 4.8 kg m^{-2} h^{-1} under a decent airflow of 2 m s^{-1}, positioning it among the best-performing solar-powered SGs to date. (iii) Demonstration of SG arrays with zero thermal loss: The arrangement and spacing of best-performing 8-Fin SG in square, circular and diamond configurations were investigated. The simulated dwell time of air particles can serve as a reliable metric for evaluating the evaporation performance of SG arrays, which was corroborated by outdoor evaporation experiments. Among the three array forms, the circular SG array with 12 cm spacing attained a water evaporation rate of 5.9 kg m^{-2} h^{-1} under natural sunlight. Remarkably, all structural components (both surface and fins) of each SG maintained

sub-ambient temperatures relative to both air and water throughout operation, achieving sustained all-cold evaporation with zero thermal losses under real-sky conditions. This study demonstrates the first example of combining numerical simulation and experimental studies for boosting solar-powered interfacial evaporation based on an integrated SG array design. It establishes a new paradigm for advancing SG arrays toward future advanced, tailored system-level applications.

EXPERIMENTAL SECTION

Fabrication of individual SGs. The balsa wood was precision-cut into cylindrical shapes with a radius of 3 cm and a height of 0.3 cm. Photothermal layers were fabricated by electrospinning commercial black polyurethane, forming nanofibrous mats that were subsequently assembled as the top surface of SGs. The balsa wood was shaped into rectangular sheets of uniform dimensions (5 cm × 1.4 cm × 0.5 cm) to construct the side fins of the SGs. Using a 3D printer, various structural frameworks were fabricated to enable the rotational positioning of the fins around the circumcenter of the upper circular surface, with angular increments of 90°, 60°, 45°, 36° and 30°. By assembling the top surface of the SG with the fin components using these 3D-printed frameworks, SGs with varying fin counts (4, 6, 8, 10 and 12) were fabricated, resulting in a modular and dismountable design.

Solar evaporation measurements. Indoor solar evaporation experiments were conducted using a xenon lamp (CEL-S500, CEAULIGHT) with an AM 1.5 G optical filter at room temperature of ~28 ℃ and a humidity of ~50%. The solar flux was calibrated using a thermopile connected to a power meter (CEL-NP2000, CEAULIGHT). The water's mass changes were real-time recorded by using a high-precision electronic balance (QUINTIX224-1CN, Sartorius, accuracy: 0.1 mg). The temperature distributions of SGs, air and water were monitored by an IR camera (223s-L19, Fotric Precision Instruments) and *k*-type thermocouples. Outdoor solar evaporation experiments were conducted in June at Ocean University of China,

Qingdao, China.

ASSOCIATED CONTENT

Supporting Information

Structural stability, absorption characterization, fiber diameter distribution, energy balance analysis, solar desalination, physical modeling, mesh generation, simulation of temperature, air velocity, RH and air particle distribution, outdoor water evaporation characterization and water quality characterization

AUTHOR INFORMATION

Corresponding Authors

Xiaofeng Xu − *College of Materials Science and Engineering, Ocean University of China, Qingdao 266100, China; Email: xuxiaofeng@ouc.edu.cn*

Zhihang Wang − *School of Engineering, College of Science and Engineering, University of Derby, Markeaton Street, Derby DE22 3AW, United Kingdom. Department of Materials Science and Metallurgy, University of Cambridge, Cambridge, CB3 0FS, United Kingdom. Email: zw428@cam.ac.uk*

Authors

Ke Shao − *College of Materials Science and Engineering, Ocean University of China, Qingdao 266100, China.*

Jingjing Li − *College of Materials Science and Engineering, Ocean University of China, Qingdao 266100, China.*

Jun Zhao − *College of Materials Science and Engineering, Ocean University of China, Qingdao 266100, China.*

Suxu Wang − *College of Materials Science and Engineering, Ocean University of China, Qingdao 266100, China.*

Yi Lu − *Jiangsu Co-Innovation Center of Efficient Processing and Utilization of Forest Resources, International Innovation Center for Forest Chemicals and Materials, College of Science, Nanjing Forestry University, Nanjing 210037, China.*

Petri Murto − *Department of Chemistry and Materials Science, Aalto University, Kemistintie 1, 02150 Espoo, Finland. Yusuf Hamied Department of Chemistry, University of Cambridge, Cambridge, CB2 1EW, United Kingdom.*

Author Contributions

Ke Shao: Methodology, Investigation, Formal analysis, Writing - original draft. **Jingjing Li:** Investigation, Software. **Jun Zhao:** Methodology, Investigation, Formal analysis. **Suxu Wang:** Investigation, Formal analysis, Data Curation. **Yi Lu:** Investigation, Data Curation. **Petri Murto:** Writing - Review & Editing, Methodology, Visualization. **Zhihang Wang:** Writing - Review & Editing, Methodology, Formal analysis. **Xiaofeng Xu:** Conceptualization, Writing - original draft, Project administration, Supervision.

Notes

The authors declare no competing financial interest.

ACKNOWLEDGMENTS

We acknowledge the financial support from the National Natural Science Foundation of China (Grant No. 22379133), the Taishan Scholar Program of Shandong Province, China (Grant No. tsqn201812026), the Natural Science Foundation of Shandong Province, China (Grant No. ZR2023MB087), and the Natural Science Foundation of Qingdao, China (Grant No. 23-2-1-243-zyyd-jch).

REFERENCES

(1) Zhang, W.; Chen, Y.; Ji, Q.; Fan, Y.; Zhang, G.; Lu, X.; Hu, C.; Liu, H.; Qu, J., Assessing global drinking water potential from electricity-free solar water evaporation device. *Nat. Commun.* **2024,** *15* (1), 6784.

(2) Mekonnen, M. M.; Hoekstra, A. Y., Four billion people facing severe water scarcity. *Sci. Adv.* **2016,** *2* (2), e1500323.
(3) Deshmukh, A.; Boo, C.; Karanikola, V.; Lin, S.; Straub, A. P.; Tong, T.; Warsinger, D. M.; Elimelech, M., Membrane distillation at the water-energy nexus: limits, opportunities, and challenges. *Energy Environ. Sci.* **2018,** *11*, 1177-1196.
(4) Ghazi, Z. M.; Rizvi, S. W. F.; Shahid, W. M.; Abdulhameed, A. M.; Saleem, H.; Zaidi, S. J., An overview of water desalination systems integrated with renewable energy sources. *Desalination* **2022,** *542*, 116063.
(5) Wei, Z.; Wang, J.; Guo, S.; Tan, S. C., Towards highly salt-rejecting solar interfacial evaporation: Photothermal materials selection, structural designs, and energy management. *Nano Res. Energy* **2022,** *1*, 9120014.
(6) Xu, N.; Li, J.; Finnerty, C.; Song, Y.; Zhou, L.; Zhu, B.; Wang, P.; Mi, B.; Zhu, J., Going beyond efficiency for solar evaporation. *Nat. Water* **2023,** *1* (6), 494-501.
(7) Wu, X.; Lu, Y.; Ren, X.; Wu, P.; Chu, D.; Yang, X.; Xu, H., Interfacial Solar Evaporation: From Fundamental Research to Applications. *Adv. Mater.* **2024,** *36* (23), 2313090.
(8) Hyeon Tae Kim; Ligy Philip; Andrew McDonagh; Md Johir; Jiawei Ren; Ho Kyong Shon; Tijing, L. D., Recent Advances in High-Rate Solar-Driven Interfacial Evaporation. *Adv. Sci.* **2024,** *11* (26), 2401322.
(9) Zhou, M.; Zhang, L.; Tao, S.; Li, R.; Wang, Y., Recent research advances in efficient solar-driven interfacial evaporation. *Chem. Eng. J.* **2024,** *489*, 151157.
(10) Yang, Z.; Li, D.; Zhu, Y.; Zhu, X.; Yu, W.; Yang, K.; Chen, B., Developing Salt-Rejecting Evaporators for Solar Desalination: A Critical Review. *Environ. Sci. Technol.* **2024,** *58* (20), 8610-8630.
(11) Geng, X.; Yang, P.; Wan, Y., How to reduce enthalpy in the interfacial solar water generation system for enhancing efficiency? *Nano Energy* **2024,** *123*, 109434.
(12) Wang, J.; Kong, Y.; Liu, Z.; Wang, H., Solar-driven interfacial evaporation: Design and application progress of structural evaporators and functional distillers. *Nano Energy* **2023,** *108*, 108115.
(13) Liang, Y.; Wang, D.; Yu, H.; Wu, X.; Lu, Y.; Yang, X.; Owens, G.; Xu, H., Recent innovations in 3D solar evaporators and their functionalities. *Sci. Bull.* **2024,** *69*, 3590–3617.
(14) Li, S.; Xiao, P.; Chen, T., Superhydrophobic Solar-to-Thermal Materials Toward Cutting-Edge Applications. *Adv. Mater.* **2024,** *36* (37), 2311453.
(15) Jin, B.; Lu, Y.; Zhang, X.; Zhang, X.; Li, D.; Liu, Q.; Deng, B.; Li, H., Iceberg-inspired solar water generator for enhanced thermoelectricity–freshwater synergistic production. *Chem. Eng. J.* **2023,** *469*, 143906.
(16) Zhu, G.; Jing, G.; Xu, G.; Li, Q.; Huang, R.; Li, F.; Li, H.; Wang, D.; Chen,

W.; Tang, B. Z., A green and efficient strategy facilitates continuous solar-induced steam generation based on tea-assisted synthesis of gold nanoflowers. *Nano Res.* **2022,** *15* (7), 6705-6712.
(17) Zheng, Z.; Li, H.; Zhang, X.; Jiang, H.; Geng, X.; Li, S.; Tu, H.; Cheng, X.; Yang, P.; Wan, Y., High-absorption solar steam device comprising Au@Bi_2MoO_6-CDs: Extraordinary desalination and electricity generation. *Nano Energy* **2020,** *68*, 104298.
(18) Li, N.; Qiao, L.; He, J.; Wang, S.; Yu, L.; Murto, P.; Li, X.; Xu, X., Solar-Driven Interfacial Evaporation and Self-Powered Water Wave Detection Based on an All-Cellulose Monolithic Design. *Adv. Funct. Mater.* **2021,** *31* (7), 2008681.
(19) Li, F.; Li, N.; Wang, S.; Qiao, L.; Yu, L.; Murto, P.; Xu, X., Self-Repairing and Damage-Tolerant Hydrogels for Efficient Solar-Powered Water Purification and Desalination. *Adv. Funct. Mater.* **2021,** *31* (40), 2104464.
(20) Li, N.; Shao, K.; He, J.; Wang, S.; Li, S.; Wu, X.; Li, J.; Guo, C.; Yu, L.; Murto, P.; Chen, J.; Xu, X., Solar-Powered Interfacial Evaporation and Deicing Based on a 3D-Printed Multiscale Hierarchical Design. *Small* **2023,** *19* (33), 2301474.
(21) Liu, M.; Sun, Y.; Shao, K.; Li, N.; Li, J.; Murto, P.; Wang, Z.; Chen, J.; Xu, X., Synergistic solar-powered water-electricity generation: An integrated floating system on water. *Nano Energy* **2024,** *119*, 109074.
(22) Abdelsalam, M. A.; Sajjad, M.; AlMarzooqi, A. R. F.; Zhang, T., Sustainable biomimetic solar distillation with edge crystallization for passive salt collection and zero brine discharge. *Nat. Commun.* **2024,** *15*, 874.
(23) Li, L.; Xue, C.; Chang, Q.; Ren, X.; Li, N.; Yang, J.; Hu, S.; Xu, H., Polyelectrolyte Hydrogel-Functionalized Photothermal Sponge Enables Simultaneously Continuous Solar Desalination and Electricity Generation without Salt Accumulation. *Adv. Mater.* **2024,** *36*, 2401171.
(24) Lei, Z.; Hu, B.; Zhu, P.; Wang, X.; Xu, B., A multilayer mesh porous 3D-felt fabric evaporator with concave array structures for high-performance solar desalination and electricity generation. *Nano Energy* **2024,** *122*, 109307.
(25) Wu, Y.; Ma, C.; Zhu, K.; Jin, L.; Song, L.; Li, L.; Lu, Y.; Zheng, Y.; Zhang, Y.; Zhen, X.; Wu, S.; Pang, Y.; Shen, Z.; Tan, S. C.; Chen, H., Asymmetric evaporation for efficient and simultaneous extraction of freshwater, salt, and electrical energy from seawater. *Energy Environ. Sci.* **2024,** *17*, 9303–9312
(26) Yu, M.-Y.; Wu, J.; Yin, G.; Jiao, F.-Z.; Yu, Z.-Z.; Qu, J., Dynamic Regulation of Hydrogen Bonding Networks and Solvation Structures for Synergistic Solar-Thermal Desalination of Seawater and Catalytic Degradation of Organic Pollutants. *Nano-Micro Lett.* **2025,** *17*, 48.
(27) Yang, H.; Li, D.; Zheng, X.; Zuo, J.; Zhao, B.; Li, D.; Zhang, J.; Liang, Z.; Jin, J.; Ju, S.; Peng, M.; Sun, Y.; Jiang, L., High Freshwater Flux Solar Desalination via a 3D Plasmonic Evaporator with an Efficient Heat-Mass

Evaporation Interface. *Adv. Mater.* **2023,** *35* (47), 2304699.
(28) Zhang, X.; Yan, Y.; Li, N.; Yang, P.; Yang, Y.; Duan, G.; Wang, X.; Xu, Y.; Li, Y., A robust and 3D-printed solar evaporator based on naturally occurring molecules. *Sci. Bull.* **2023,** *68*, 203–213.
(29) Liang, Y.; Wang, D.; Yu, H.; Wu, X.; Lu, Y.; Yang, X.; Owens, G.; Xu, H., Recent innovations in 3D solar evaporators and their functionalities. *Sci. Bull.* **2024,** *69* (22), 3590-3617.
(30) Liao, Y.; Wang, C.; Dong, Y.; Miao, Z.; Yu, H.-Y.; Chen, G.; Yao, J.; Zhou, Y.; Liu, Y., Spherical Design-Driven Scalable Solar-Powered Water Treatment with Salt Self-Cleaning and Light Self-Adaptivity. *Adv. Funct. Mater.* **2024,** *34* (51), 2409813.
(31) Gao, T.; Wang, Y.; Wu, X.; Wu, P.; Yang, X.; Li, Q.; Zhang, Z.; Zhang, D.; Owens, G.; Xu, H., More from less: improving solar steam generation by selectively removing a portion of evaporation surface. *Sci. Bull.* **2022,** *67* (15), 1572-1580.
(32) Dai, C.; Li, Z.; Zheng, K.; Zhang, J.-H.; Dai, R.; Luo, D.; Gao, H.; Thabet, H. K.; El-Bahy, Z. M.; Pan, L.; Mai, Y.; Yamauchi, Y.; Xu, X., Strategic design of porous interfacial evaporators: A comprehensive review unveiling the significant role of pore engineering. *Nano Energy* **2024,** *131*, 110244.
(33) Wei, Y.; Yang, Y.; Zhao, Q.; Ma, Y.; Qiang, M.; Fu, L.; Liu, Y.; Zhang, J.; Qu, Z.; Que, W., Numerical Simulation Technologies in Solar-Driven Interfacial Evaporation Processes. *Small* **2024,** *20* (32), 2312241.
(34) Wang, Y.; Wu, X.; Yang, X.; Owens, G.; Xu, H., Reversing heat conduction loss: Extracting energy from bulk water to enhance solar steam generation. *Nano Energy* **2020,** *78*, 105269.
(35) Wang, Y.; Wu, X.; Wu, P.; Zhao, J.; Yang, X.; Owens, G.; Xu, H., Enhancing solar steam generation using a highly thermally conductive evaporator support. *Sci. Bull.* **2021,** *66* (24), 2479-2488.
(36) Zhang, L.; Li, X.; Zhong, Y.; Leroy, A.; Xu, Z.; Zhao, L.; Wang, E. N., Highly efficient and salt rejecting solar evaporation via a wick-free confined water layer. *Nat. Commun.* **2022,** *13* (1), 849.
(37) Deng, W.; Fan, T.; Li, Y., Water wave vibration-promoted solar evaporation with super high productivity. *Nano Energy* **2022,** *92*, 106745.
(38) Wang, Y.; Shang, Y.; Sun, X.; Yang, Q.; Zhang, Y., Enhancing Freshwater Production via Customizable and Highly Efficient Solar-Driven Seawater Desalination. *ACS Appl. Mater. Interfaces* **2023,** *15* (34), 40595-40605.
(39) Zou, M.; Zhang, Y.; Cai, Z.; Li, C.; Sun, Z.; Yu, C.; Dong, Z.; Wu, L.; Song, Y., 3D Printing a Biomimetic Bridge-Arch Solar Evaporator for Eliminating Salt Accumulation with Desalination and Agricultural Applications. *Adv. Mater.* **2021,** *33* (34), 2102443.
(40) Liu, X.; Chen, F.; Li, Y.; Jiang, H.; Mishra, D. D.; Yu, F.; Chen, Z.; Hu, C.; Chen, Y.; Qu, L.; Zheng, W., 3D Hydrogel Evaporator with Vertical Radiant

Vessels Breaking the Trade-Off between Thermal Localization and Salt Resistance for Solar Desalination of High-Salinity. *Adv. Mater.* **2022,** *34* (36), 2203137.
(41) Lee, W. H.; Lee, C. W.; Cha, G. D.; Lee, B.-H.; Jeong, J. H.; Park, H.; Heo, J.; Bootharaju, M. S.; Sunwoo, S.-H.; Kim, J. H.; Ahn, K. H.; Kim, D.-H.; Hyeon, T., Floatable photocatalytic hydrogel nanocomposites for large-scale solar hydrogen production. *Nat. Nano.* **2023,** *18* (7), 754-762.
(42) Wei, D.; Wang, C.; Shi, G.; Zhang, J.; Wang, F.; Tan, P.; Zhao, Z.; Xie, Y., Enabling Self-Adaptive Water-Energy-Balance of Photothermal Water Diode Evaporator: Dynamically Maximizing Energy Utilization Under the Ever-Changing Sunlight. *Adv. Mater.* **2024,** *36* (18), 2309507.
(43) Lu, Y.; Fan, D.; Wang, Y.; Xu, H.; Lu, C.; Yang, X., Surface Patterning of Two-Dimensional Nanostructure-Embedded Photothermal Hydrogels for High-Yield Solar Steam Generation. *ACS Nano* **2021,** *15* (6), 10366-10376.
(44) Yang, H.; Sun, Y.; Peng, M.; Cai, M.; Zhao, B.; Li, D.; Liang, Z.; Jiang, L., Tailoring the Salt Transport Flux of Solar Evaporators for a Highly Effective Salt-Resistant Desalination with High Productivity. *ACS Nano* **2022,** *16* (2), 2511-2520.
(45) Yang, Y.; Feng, H.; Que, W.; Qiu, Y.; Li, Y.; Guo, L.; Li, Q., A Diode-like Scalable Asymmetric Solar Evaporator with Ultra-high Salt Resistance. *Adv. Funct. Mater.* **2023,** *33* (6), 2210972.
(46) Li, M.; Liu, B.; Liu, Z.; Xiao, Y.; Guo, H.; An, Z.; Wang, L.; James, T. D., Reducing Heat Conduction Enhances the Photothermal Efficiency of Upcycled Adsorbents. *Adv. Funct. Mater.* **2023,** *33* (4), 2209987.
(47) Jin, B.; Lu, Y.; Zhang, X.; Zhang, X.; Li, D.; Liu, Q.; Deng, B.; Li, H., Iceberg-inspired solar water generator for enhanced thermoelectricity–freshwater synergistic production. *Chem. Eng. J.* **2023,** *469*, 143906.
(48) He, N.; Sun, X.; Wang, H.; Wang, B.; Tang, D.; Li, L., Dual-Interface Solar Evaporator with Highly-Efficient Thermal Regulation via Suspended Multilayer Design. *Small* **2024,** *20* (38), 2402863.
(49) Zhao, D.; Ding, M.; Lin, T.; Duan, Z.; Wei, R.; Feng, P.; Yu, J.; Liu, C.-Y.; Li, C., Gradient Graphene Spiral Sponges for Efficient Solar Evaporation and Zero Liquid Discharge Desalination with Directional Salt Crystallization. *Adv. Sci.* **2024,** *11* (22), 2400310.
(50) Ren, L.; Zhang, Q.; Zhao, G.; Chen, T.; Wang, Y.; Xiao, X.; Yang, H.; Xu, N.; Xu, W., Interconnected Porous Fabric-Based Scalable Evaporator with Asymmetric Wetting Properties for High-Yield and Salt-Rejecting Solar Brine Treatment. *Adv. Fiber Mater.* **2024,** *6* (4), 1162-1173.
(51) Hu, Y.; Li, S.; Zhuang, W.; Tu, H.; Wan, Y.; Yang, P., Spatial Patterned Interfacial Solar Evaporators toward Recovering Heat Loss. *ACS Appl. Mater. Interfaces* **2024,** *16* (8), 10285-10294.
(52) Wang, H.; Wang, Z.; Wang, T.; Tang, W.; Gao, S.; Niu, H.; Yin, Y.; Yin, X.;

Wu, T., Shooting Three Birds with One Stone: Device Construction and Thermal Management for Simultaneous Photothermal Conversion Water Evaporation, Thermoelectric Generation and Photocatalytic Degradation. *Adv. Funct. Mater.* **2024,** *34* (23), 2315211.

(53) Zheng, S. Y.; Zhou, J.; Si, M.; Wang, S.; Zhu, F.; Lin, J.; Fu, J.; Zhang, D.; Yang, J., A Molecularly Engineered Zwitterionic Hydrogel with Strengthened Anti-Polyelectrolyte Effect: from High-Rate Solar Desalination to Efficient Electricity Generation. *Adv. Funct. Mater.* **2023,** *33* (43), 2303272.

(54) Yu, H.; Wang, D.; Jin, H.; Wu, P.; Wu, X.; Chu, D.; Lu, Y.; Xiaofei Yang; Xu, H., 2D $MoN_{1.2}$-rGO Stacked Heterostructures Enabled Water State Modification for Highly Efficient Interfacial Solar Evaporation. *Adv. Funct. Mater.* **2023,** *33* (24), 2214828.

(55) Yu, H.; Jin, H.; Qiu, M.; Liang, Y.; Sun, P.; Cheng, C.; Wu, P.; Wang, Y.; Wu, X.; Chu, D.; Zheng, M.; Qiu, T.; Lu, Y.; Zhang, B.; Mai, W.; Yang, X.; Owens, G.; Xu, H., Making Interfacial Solar Evaporation of Seawater Faster than Fresh Water. *Adv. Mater.* **2024**, *36* (52), 2414045.

(56) Li, W.; Zheng, Z.; Qian, Z.; Liu, H.; Wang, X., Phase Change Material Boosting Electricity Output and Freshwater Production through Hierarchical-Structured 3D Solar Evaporator. *Adv. Funct. Mater.* **2024,** *34* (26), 2316504.

(57) Dang, C.; Cao, Y.; Nie, H.; Lang, W.; Zhang, J.; Xu, G.; Zhu, M., Structure integration and architecture of solar-driven interfacial desalination from miniaturization designs to industrial applications. *Nat. Water* **2024,** *2* (2), 115-126.

(58) Zhang, L.; Liu, G.; Wu, L.; Chen, Z.; Dai, Z.; Yu, F.; Wang, X., Integrated light adsorption and thermal insulation of Zn doping 1T phase MoS_2-based evaporation prototype for continuous freshwater generation. *Chem. Eng. J.* **2023,** *454*, 140298.

(59) Zhang, L.; Zhang, Y.; Zou, M.; Yu, C.; Li, C.; Gao, C.; Dong, Z.; Wu, L.; Song, Y., A Bionic-Gill 3D Hydrogel Evaporator with Multidirectional Crossflow Salt Mitigation and Aquaculture Applications. *Adv. Funct. Mater.* **2023,** *33* (24), 2300318.

(60) Li, T.; Liu, H.; Zhao, X.; Chen, G.; Dai, J.; Pastel, G.; Jia, C.; Chen, C.; Hitz, E.; Siddhartha, D.; Yang, R.; Hu, L., Scalable and Highly Efficient Mesoporous Wood-Based Solar Steam Generation Device: Localized Heat, Rapid Water Transport. *Adv. Funct. Mater.* **2018,** *28* (16), 1707134.

(61) Kuang, Y.; Chen, C.; He, S.; Hitz, E. M.; Wang, Y.; Gan, W.; Mi, R.; Hu, L., A High-Performance Self-Regenerating Solar Evaporator for Continuous Water Desalination. *Adv. Mater.* **2019,** *31* (23), 1900498.

(62) Dong, X.; Cao, L.; Si, Y.; Ding, B.; Deng, H., Cellular Structured CNTs@SiO_2 Nanofibrous Aerogels with Vertically Aligned Vessels for Salt-

Resistant Solar Desalination. *Adv. Mater.* **2020,** *32* (34), 1908269.
(63) Li, X.; Ni, G.; Cooper, T.; Xu, N.; Li, J.; Zhou, L.; Hu, X.; Zhu, B.; Yao, P.; Zhu, J., Measuring Conversion Efficiency of Solar Vapor Generation. *Joule* **2019,** *3* (8), 1798-1803.
(64) Bu, Y.; Zhou, Y.; Lei, W.; Ren, L.; Xiao, J.; Yang, H.; Xu, W.; Li, J., A bioinspired 3D solar evaporator with balanced water supply and evaporation for highly efficient photothermal steam generation. *J. Mater. Chem. A,* **2022,** *10*, 2856–2866.
(65) Gu, X.; Dong, K.; Peng, L.; Bian, L.; Sun, Q.; Luo, W.; Zhang, B., Round-the-clock interfacial solar vapor generator enabled by form-stable phase change materials with enhanced photothermal conversion capacity. *Energy Convers. Manage.* **2023,** *277*, 116634.
(66) Chen, Y.; Wang, Y.; Xu, J.; Ibn Raihan, M. R.; Guo, B.; Yang, G.; Li, M.; Bao, H.; Xu, H., A 3D Opened Hollow Photothermal Evaporator for Highly Efficient Solar Steam Generation. *Sol. RRL* **2022,** *6* (7), 2200202.
(67) Chen, Y.; Hao, J.; Xu, J.; Hu, Z.; Bao, H.; Xu, H., Pickering Emulsion Templated 3D Cylindrical Open Porous Aerogel for Highly Efficient Solar Steam Generation. *Small* **2023,** *19* (48), 2303908.
(68) Zhang, L.; Li, X.; Zhong, Y.; Leroy, A.; Zhenyuan; Zhao, L.; Wang, E. N., Highly efficient and salt rejecting solar evaporation via a wick-free confined water layer. *Nat. Commun.* **2022,** *13*, 849.
(69) Wu, X.; Wu, Z.; Wang, Y.; Gao, T.; Li, Q.; Xu, H., All-Cold Evaporation under One Sun with Zero Energy Loss by Using a Heatsink Inspired Solar Evaporator. *Adv. Sci.* **2021,** *8 (7)*, 2002501.
(70) Chen, M.; Li, S.; Guo, S.; Yan, H.; Tan, S. C., Recent advances in water collection based on solar evaporation. *Green Energy Environ.* **2024,** *9* (12), 1812-1821.

Table of Contents

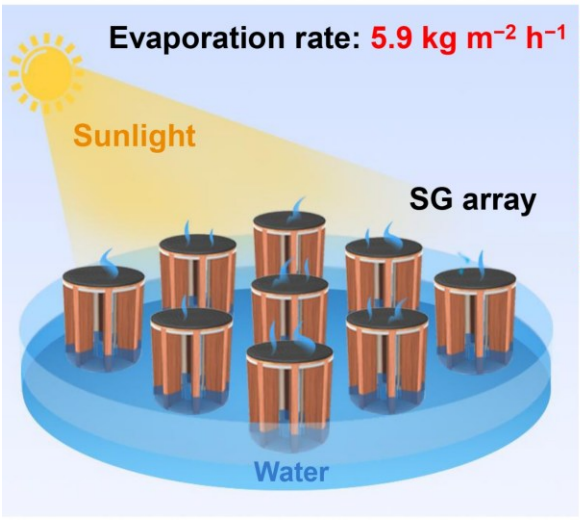

Design from one SG to a SG array

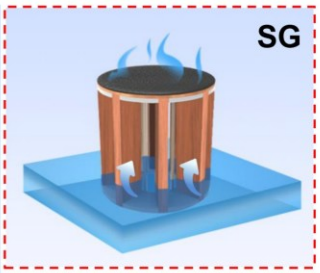

Modular SG

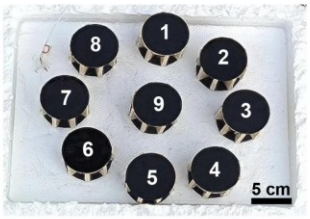

SG arrangement

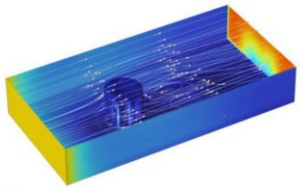

Multiphysics simulation

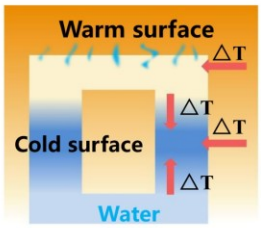

All-cold evaporation